



## Filling simulation of the RTM process in isotropic homogeneous/non-homogeneous media using the boundary element method

J.D. Vanegas & I.D. Patiño

To cite this article: J.D. Vanegas & I.D. Patiño (2015) Filling simulation of the RTM process in isotropic homogeneous/non-homogeneous media using the boundary element method, *Advanced Composite Materials*, 24:2, 113-139, DOI: [10.1080/09243046.2013.879401](https://doi.org/10.1080/09243046.2013.879401)

To link to this article: <http://dx.doi.org/10.1080/09243046.2013.879401>



Published online: 05 Feb 2014.



Submit your article to this journal [↗](#)



Article views: 61



View related articles [↗](#)



View Crossmark data [↗](#)



## Filling simulation of the RTM process in isotropic homogeneous/non-homogeneous media using the boundary element method

J.D. Vanegas\* and I.D. Patiño

*Grupo de Investigación Materiales Avanzados y Energía, Línea Materiales Poliméricos, Sublínea Composites, Instituto Tecnológico Metropolitano (ITM), Medellín, Colombia*

*(Received 2 July 2013; accepted 25 December 2013)*

Two Boundary Element Method (BEM) approaches are implemented in the simulation of the filling of isotropic fiber-reinforced preforms used in Resin Transfer Molding (RTM). One is a pure BEM approach used in homogeneous domains where the permeability remains constant in the space; the other one is a Dual reciprocity boundary element method (DR-BEM) approach employed in non-homogeneous domains where the permeability changes as a known function. Five cases are briefly discussed: the first two cases deal with a homogeneous domain and piecewise constant pressure and constant flow regimes; the third case considers gravitational effects in a constant pressure injection conducted in a homogeneous domain; the last two cases deal with constant pressure and constant flow injections in a non-homogeneous domain where the permeability changes in radial form. The accuracy of the BEM approaches is evaluated by comparing the numerical results obtained in the simulations with analytical, experimental and numerical results of other authors. In addition to the accuracy assessment of the approaches implemented, in the present research, both flow regimes for the same homogeneous domain are compared and the influence of the change of the fiber volume fraction presented in the non-homogeneous domain is analyzed on the behavior of the radial pressure profile.

**Keywords:** liquid composite molding; boundary element method; filling simulation

### 1. Introduction

The resin transfer molding process (RTM) is widely used in the manufacturing of composites parts in many types of industries. This process can be summarized into four principal steps: cutting and positioning of the reinforcement preforms inside the mold, injection of the catalyzed resin once the mold is correctly closed and sealed (the injection can be vacuum assisted), and curing of the resin and demolding of the part. Several phenomena occur during the development of those steps: draping, impregnation at different scales, encountered flows, porosities and dry spots formation, heating and cooling of the resin and subsequent dilatations and contractions of the part, and appearance of residual stresses, among others. Some techniques have been used to simulate those phenomena and establish the set points of the processing variables to obtain high quality parts in industrial applications. In the particular case of the filling phenomenon, several simulation techniques have been employed: the finite difference method for 2D geometries with very regular boundaries,[1,2] a pure finite element

---

\*Corresponding author. Email: [jdvanegas@go-composites.com](mailto:jdvanegas@go-composites.com)

technique accounting for the transient effects,[3,4] the FEM/CV conforming technique that solves the governing equations for the pressure field using the finite element method and track the flow front advancement using a control volume scheme,[5–8] and states the basis of the algorithm of the software LIMS<sup>TM</sup> [9]; the FEM/CV non-conforming technique [10–13] has also been widely used and that is the base of the algorithm of the software PAM-RTM<sup>TM</sup>. [14] They can be also mentioned for some domain meshless techniques such as: the Boundary Element Method (BEM) method combined with the marker particle technique [15,16] or with the level set technique to track the flow front advancement for both isotropic [17] and anisotropic preforms,[18] the BEM method combined with perturbation techniques for the simulation of isotropic preforms and heterogeneous domains,[19] the natural element method,[20–22] and the smoothed particle hydrodynamic technique.[23] The main advantage of the BEM-based techniques over traditional domain mesh methods, such as FEM/CV, is that the saturated domain does not need a mesh for the solution of the governing equations; only a mesh of the surrounding surface is needed, thus reducing the solution of the problem in one dimension regarding to the original dimension. This entails a reduction in the computational cost of the simulation until a determined mesh size, as it was demonstrated by Soukane and Trochu [17]. Additionally, BEM-based techniques can be combined with other numerical techniques to track the flow front interface; those techniques do not imply the updating of the fill factors of control volumes, which is proper of the VOF technique, and some of them are the marker particle technique [19] and the level set technique [18]; to obviate the updating of fill factors can also contribute to the reduction of the computational cost when those techniques are implemented in correct form for determined applications.

In the present work, they are considered as two techniques to simulate the filling of isotropic preforms. The first one is a pure BEM technique,[24] used here for the simulation of homogeneous domains; the principal difference of the present approach employing this technique with other works,[17,18] regarding to the solution of the governing equations, is the discretization of the boundary in quadratic elements instead of linear ones, the computations of normals from the cloud of points using Catmull Rom splines [25] and the use of a different fundamental solutions including a reference radius.[26] The second technique is the Dual reciprocity boundary element method (DR-BEM), used here for the simulation of heterogeneous domains and that consists on the treatment by the dual reciprocity method [27] of the domain integral that arises on the integral formulation of the problem. The first three cases of the present work deal with homogeneous domains and consider separately a piecewise constant pressure regime (case one), a constant flow regime (case two) and a constant pressure regime with gravitational effects (case three). The other two cases correspond to the infiltration of heterogeneous domains, where the variation of the permeability can be approximated by a continuous function of the spatial coordinates; both constant pressure (case four) and constant flow regime (case five) are considered in that heterogeneous domain. The accuracy of the algorithm developed in MATLAB<sup>TM</sup> is evaluated by comparison of some numerical results to analytical and experimental results. Based on the numerical results of the present approach, a comparison among both injection regimes for the homogeneous domain is made, as well as it is analyzed that the influence of the variation of the fiber volume fraction presented in the heterogeneous domain on the behavior of the pressure profiles with time. The influence of the gravitational effects on the flow fronts is also dealt with using the numerical results.

## 2. Governing equations and numerical treatment by DR-BEM

In the bi-dimensional case and considering the superficial velocity of the flow front, the governing equation of the pressure field for darcian, isotropic, and heterogeneous porous media is the following:

$$\frac{\partial}{\partial x_i} \left( K(x) \frac{\partial \theta(x)}{\partial x_i} \right) = 0 \quad (1)$$

To deal with Equation (1) by boundary element techniques, this equation shall be transformed to a Poisson equation employing a transformation used by other authors for other kind of problems.[28,29] This transformation is shown in the Equation (2) and the resulting Poisson equation is the expression (3), where  $u$  is the transformed potential and  $g(x_1, x_2) = |\nabla K(x_1, x_2)|^2 / (4K^2(x_1, x_2)) - \nabla^2 K(x_1, x_2) / (2 \cdot K(x_1, x_2))$ .

$$u = [K(x_1, x_2)]^{1/2} \theta(x_1, x_2) \quad (2)$$

$$\nabla^2 u(x_1, x_2) + g(x_1, x_2) \cdot u(x_1, x_2) = 0 \quad (3)$$

The integral formulation of the Equation (3) is presented in the expression (4).[26]

$$c(\xi)u(\xi) = \int_S \left( u^*(\xi, \mathbf{x}) \frac{\partial u(\mathbf{x})}{\partial n_x} - u(\mathbf{x}) \frac{\partial u^*(\xi, \mathbf{x})}{\partial n_x} \right) dS_x + \int_\Omega g(x_1, x_2) u \cdot u^* d\Omega \quad (4)$$

where  $\xi$  is the source point,  $\mathbf{x}$  is the field point, and  $c(\xi) = \alpha/2\pi$ , where  $\alpha$  is the angle of the boundary contour in the source point  $\xi$ ;  $u^*(\xi, \mathbf{x}) = (1/2\pi) \cdot \ln(r_o/r^*)$  is the fundamental solution used in this work,[26] where  $r_o$  is the radius of reference, taking in this case as the inlet radius of the preforms.

As it can be seen in the integral Equation (4), a domain integral arises because of the variation of the permeability,  $K(x_1, x_2)$ , in the space of the porous medium. Applying the dual-reciprocity method to that domain integral,[27,28] the Equation (4) changes into:

$$\begin{aligned} c(\xi)u(\xi) - \int_S (u^*(\xi, \mathbf{x})q(\mathbf{x}) - u(\mathbf{x})q^*(\xi, \mathbf{x})) dS_x \\ = \sum_{j=1}^{N+L} \alpha_j \left( c(\xi)\hat{u}_j(\xi) - \int_S (u^*(\xi, \mathbf{x})\hat{q}_j(\mathbf{x}) - \hat{u}_j(\mathbf{x})q^*(\xi, \mathbf{x})) dS_x \right) \end{aligned} \quad (5)$$

where

$$q(\mathbf{x}) = \partial u(\mathbf{x}) / \partial n_x$$

$$q^*(\xi, \mathbf{x}) = \partial u^*(\xi, \mathbf{x}) / \partial n_x = -(1/2\pi) \cdot (r^*)^{-2} \cdot [(x_1 - \xi_1) \cdot n_1 + (x_2 - \xi_2) \cdot n_2]$$

$$\alpha_j \text{ are defined by the next equation: } -g(x_1, x_2) \cdot u(x_1, x_2) = \sum_{j=1}^{N+L} \alpha_j \cdot f_j$$

$$f_j = (r^*)^2 \ln(r^*): \text{Thin plate splines approximation functions.}$$

$$\hat{u}_j(\mathbf{x}) = \frac{1}{16} (r^*)^4 \ln(r^*) - \frac{1}{32} (r^*)^4: \text{Adjacent harmonic functions for thin plate splines.}$$

$$\hat{q}_j(\mathbf{x}) = \partial \hat{u}_j(\mathbf{x}) / \partial n = (1/16) (r^*)^2 \cdot (4 \cdot \ln(r^*) - 1) \cdot [(x_1^j - x_1) \cdot n_1 + (x_2^j - x_2) \cdot n_2]$$

where  $(x_1^j, x_2^j)$  represents the 'N+L' DR- BEM collocation points.

The location of the collocation points inside the domain are established in such a way that concentric circles are formed by those points and the distance among two adjacent circles has a maximum value of  $r = 6 \text{ mm}$ .

### 3. Boundary conditions and outputs

The boundary conditions in the problem of infiltration of fiber reinforcements by resin depend on the flow regime. In constant pressure regime, the boundary conditions are of Dirichlet type, the injection pressure and the zero or vacuum pressure being the most common conditions in the inlet and the flow front, respectively. Gravitational effects can be taken into account in the boundary conditions. The general form of the Dirichlet boundary conditions in this kind of problems is:  $\bar{\phi} = p + \rho g z$ , where the upper LINE represents a prescribed value. Introducing the change of variable of the Equation (2), the original boundary condition change into:  $\bar{u}(x_1, x_2) = [K(x_1, x_2)]^{1/2} \bar{\phi}$ .

For constant flow regimes, the boundary conditions in the inlet are of Neumann type. For a determined point in the inlet, the flow of potential in the normal direction,  $\bar{q}_{in}$ , can be calculated in terms of the injected flow rate ( $Q$ ), the reference radius ( $r_o$ ), the thickness of mold ( $h$ ), the permeability in the considered point ( $K(x_1, x_2)$ ), and in terms of the viscosity of the injected liquid ( $\mu$ ) using  $\bar{q}_{in}(x_1, x_2) = -[Q\mu/(2\pi \cdot r_o \cdot h)]/K(x_1, x_2)$ . In the transformed system, the inlet boundary condition is converted into a Robin boundary condition:  $\partial u_{in}/\partial n = 1/(2K(x_1, x_2)) \cdot (\partial K(x_1, x_2)/\partial n) \cdot u_{in} + (K(x_1, x_2))^{1/2} \cdot \bar{q}_{in}(x_1, x_2)$ .

A schematic illustration of the physical phenomenon and the boundary conditions analyzed in the present work is shown in the Figure 1.

The outputs of the BEM and DR-BEM codes also depend on the flow regime. In such a manner that for constant pressure regimes, the outputs are:  $N$  values of the flow of potential on the boundary points and  $L$  values of the potential in the interior points; for constant flow regimes, the outputs are:  $N_{in}$  values of the potential on the inlet boundary points,  $N_f$  values of the flow of potential on the boundary points in the flow front, and  $L$  values of the potential in the interior points. Once the flow of potential in any point,  $\partial\phi/\partial n$ , is known, the pore velocity in the normal direction can be obtained from the Darcy's law [30]:

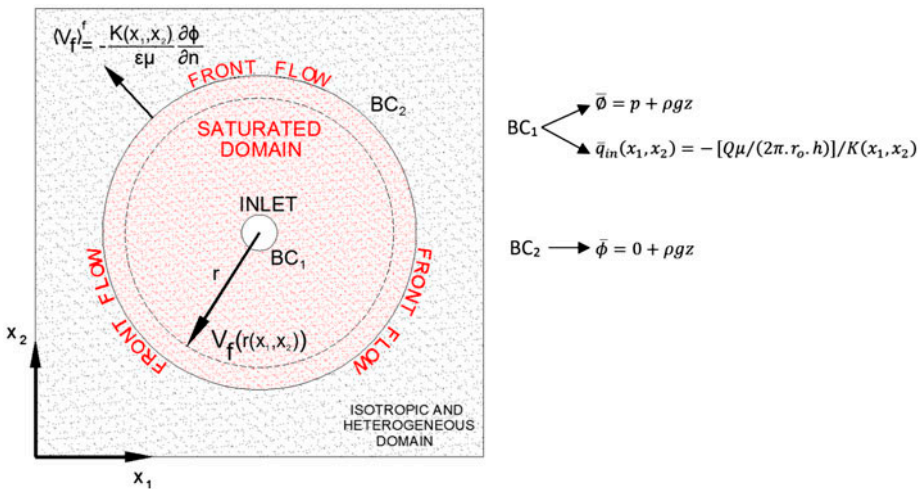


Figure 1. Phenomena schematic illustration.

$$\langle V_f \rangle^f = - \frac{K(x_1, x_2)}{\varepsilon \mu} \frac{\partial \phi}{\partial n} \quad (6)$$

#### 4. Flow front tracking

Simple radial divergent injections were simulated in order to compare the numerical results given by the present BEM approaches to analytical and experimental results and so as to analyze the influence of the pressure regime, of the gravitational effects and of the change of the fiber volume fraction on the flow front positions, on the inlet pressure history and on the velocity and pressure profiles. Because of what those simulations do not involve encountered flows or inserts, the simple technique of marker particles can be used to track the flow front advancement in the present work.[17] Further researches will be done with the purpose of combining more refined flow tracking techniques [31,32] with the present BEM approaches. In the marker particles technique, the positions are updated using an explicit finite difference scheme, as it is shown in the Equations (7) and (8), and applying the bi-dimensional CFL condition for the time interval:

$\Delta t \leq C_{\max} / \left[ \left( \langle V_f \rangle^f \cdot n_x \right) / \Delta x_t + \left( \langle V_f \rangle^f \cdot n_y \right) / \Delta y_t \right]$ , where  $C_{\max}$  depends on the instant time.

$$(x_{t+\Delta t} - x_t) / \Delta t = \langle V_f \rangle^f \cdot n_x \quad (7)$$

$$(y_{t+\Delta t} - y_t) / \Delta t = \langle V_f \rangle^f \cdot n_y \quad (8)$$

#### 5. Experimental procedures

Two kinds of injection tests were carried out in the present investigation with silicone oil. In first, the permeabilities of the cloths employed were measured by means of a unidirectional mold. The measurements were conducted by the unsaturated method [33] and the permeabilities reported are the interpolated ones.[34] The other kind of experiments consisted of divergent radial injections using a setup designed in-house. This montage comprises an injection system with a pressurizable pot, a monolithic body with a cavity for positioning of the preforms with an adequate seal system, a visual lid made of acrylic where an acetate paper with circular marks is attached for measurement purposes, a clamping system consisting on perimeter screws that hold the lid and the body together in the correct position to guarantee the thickness of the stacking during all experiment, and also a pressure sensor of range 0–10 psi located at the inlet of the liquid and a digital camera Canon 60D with lens Canon EF-S 18–55 mm adapted to capture the flow front advancement. The general scheme of the designed montage is shown in Figure 2.

The procedure of the radial divergent tests is simple: Once the reinforcement preforms and the measurement acetate are correctly positioned, the chronometer is turned on; when no movement appears in the camera, the inlet port is opened and the capture of the images starts. The time at which the liquid initially touches the preforms is registered as the reference time and this is considered the initial time of the simulation. The injection is conducted and several captures are done; using the pictures taken, the positions obtained at several times are compared with the simulation results. The

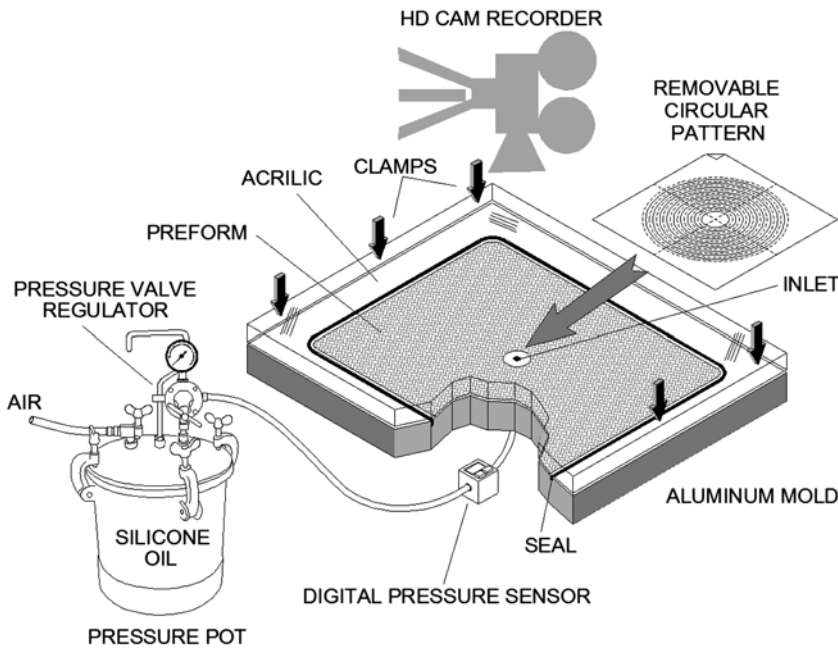


Figure 2. Scheme of experimental setup.

curve of *Viscosity vs. Temperature* of the silicone oil was obtained using a Brookfield viscometer of reference LVDV-II+PRO equipped with a thermostated circulating bath of reference TC-502P and a small sample adapter (SSA) with capacity of 16 ml.

## 6. Cases of studies

In the present work, both homogeneous and heterogeneous domains conformed of isotropic fiber reinforcements have been analyzed. Five simulation experiments with the BEM and DR-BEM codes designed were conducted: (one) Homogeneous domain–Piecewise constant pressure, (two) Homogeneous domain–Constant flow, (three) Homogeneous domain–Constant pressure with gravitational effects, (four) Heterogeneous domain–Constant pressure, and (five) Heterogeneous domain–Constant flow. The results of the simulations in (one) and (four) were compared with experimental results. In Table 1, they are given as the material, geometric, and processing parameters used in the simulations (one) and (two). The parameters of simulation (three) are shown in the Table 2, while in the Table 3, the parameters for the simulations (four) and (five) are exposed.

The inlet pressures of cases (one) and (four) matches with the values measured in the experiments. The inlet flow of cases (two) and (five) was selected in such a way that the saturated domain of the constant flow regime in the first instants of time coincides with the saturated domain of the constant pressure regime, keeping constants the other parameters. The data of Table 2 were obtained in studies carried out by Gantois et al. [18].

Table 1. Parameters for the simulation of cases one and two: homogeneous domain.

<i>Material parameters</i>						
Reinforced material	Type		Permeability @ $V_f=43.5\%$	Liquid material	Viscosity@15 °C	Density
			(m <sup>2</sup> )		(cPs)	(kg/m <sup>3</sup> )
Fiberglass	Continuous filament random MAT		$3.714 \times 10^{-10}$	Silicon oil	120	964
<i>Geometric parameters</i>						
Radius of reference, $r_o$ (mm)				Thickness of mold (mm)		
20				4.13		
<i>Processing parameters</i>						
Fiber volume fraction	Piecewise constant pressure (Pa)				Constant inlet flow (m <sup>3</sup> /s)	
43.5%	$t \in [0, 4] \text{ s}$ 5516–9653	$t \in [5, 15] \text{ s}$ 9653	$t \in [16, 56] \text{ s}$ 11,032	$t \in [57.92] \text{ s}$ 12,410	$4.94 \times 10^{-6}$	



Table 2. Parameters for the simulation of case three: Homogenous domain with gravitational effects [18].

Material parameters					
Reinforced material	Type	Permeability @ $V_f=43.5\%$ (m <sup>2</sup> )	Liquid material	Viscosity@15 °C (cPs)	Density (kg/m <sup>3</sup> )
Not reported	Not reported	$1.000 \times 10^{-9}$	Not reported	100	1150
Geometric parameters					
Radius of reference, $r_o$ (mm)			Thickness of mold (mm)		
2.5			Not reported		
Processing parameters					
Fiber volume fraction	Constant pressure in inlet and flow front (Pa)				
50%	$P_{in} = 2 \times 10^5$		$P_f = 1 \times 10^5$		

## 7. Permeability function in the heterogeneous domain

To establish a function of permeability  $K(x_1, x_2)$  in terms of the spatial coordinates, this property is represented by the equation of Kozeny-Carman:

$$K = (r_f^2/4k) \cdot (1 - V_f)^3/V_f^2 \quad (9)$$

The term  $r_f^2/4k$  can be estimated experimentally by means of the measurements of permeability at several fiber volume fractions. For the cases (four) and (five) of heterogeneous domain, measurements of permeability for a chopped strand MAT preform were conducted at the following fiber volume fractions: 17.5, 25.7, 36.2, 45.5, and 55.1%. In Table 4, they exposed the values of the permeabilities and of the terms  $r_f^2/4k$  for the mentioned fiber volume fractions. Figure 3 represents the change of  $r_f^2/4k$  with  $V_f$  and the second-order polynomial curve that better fits to the data by the least-square method. The behavior of  $r_f^2/4k$  with the fiber volume fraction is strongly dependent on the architecture of the preform. For instance, for the anisotropic fabric used in [35], the term  $r_f^2/4k$  decreases always with  $V_f$  for a range of  $V_f \in [0.342, 0.571]$ , while this term increases always in the preform used by Gutowski.[36]

The heterogeneous domain in the radial mold was created by positioning eight rectangular preforms of the same size of the cavity and then, by adding sixteen circular preforms, varying the diameter in such a way that the radial difference between adjacent preforms keeps constant in 5 mm (see Figures 4 and 5). The cloth used is chopped strand MAT, whose areal weight is taking as the average of all areal weights obtained experimentally in the twenty-four preforms employed; this value is 225.21 g per square meter. Because of the low areal weight of the preform used and considering that the radial distance between adjacent preforms is small enough ( $e = 5$  mm), the variation of the fiber volume fraction from the reference radius,  $r_o$ , to the radius of the last circular preform can be approximated by a linear function, as it is depicted in Figure 5. Therefore, the radial variation of the fiber volume fraction can be described by the next equation:

$$V_f(r) = m(r - r_o) + V_{f,o} \quad (10)$$

Table 3. Parameters for the simulation of cases four and five: Heterogeneous domain.

<i>Material parameters</i>				
Reinforced material	Type	Permeability @ $V_f=43.5\%$ ( $\text{m}^2$ )	Liquid material	Viscosity@15 °C (cPs)
Fiberglass	Chopped strand MAT	$K_{\text{max}}(V_f = 17.46\%) = 2.580 \times 10^{-9}$ $K_{\text{min}}(V_f = 52.37\%) = 7.399 \times 10^{-11}$	Silicon oil	120
<i>Geometric parameters</i>				
Radius of reference, $r_o$ (mm)			Thickness of mold (mm)	
20			4.13	
<i>Processing parameters</i>				
Fiber volume fraction	Constant pressure (Pa)			Constant inlet flow ( $\text{m}^3/\text{s}$ )
Min: 17.46%, Max: 52.37%	16, 547			$3.27 \times 10^{-6}$

Table 4. Values of permeabilities and  $r_f^2/4k$  for several fiber volume fractions.

$V_f$	Measurements of permeability (m <sup>2</sup> )	Average permeability (m <sup>2</sup> )	$r_f^2/4k$
0.551	4.602E-11 4.913E-11	4.757E-11	1.596E-10
0.455	1.931E-10 1.802E-10	1.867E-10	2.387E-10
0.362	5.079E-10 5.250E-10	5.164E-10	2.606E-10
0.257	1.456E-09 1.311E-09	1.383E-09	2.228E-10
0.175	2.503E-09 2.610E-09	2.557E-09	1.394E-10

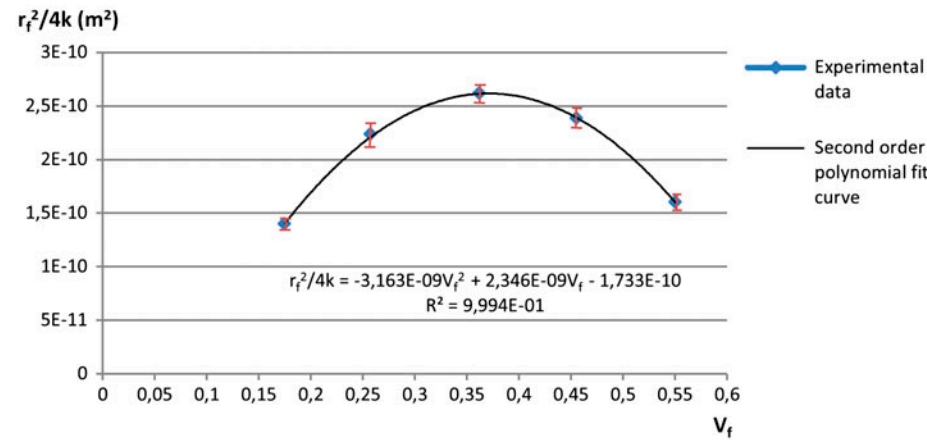


Figure 3. Change of  $r_f^2/4k$  with  $V_f$ .

where  $V_f(r)$  is the fiber volume fraction at determined radial position,  $r_o$  is the reference radius,  $m$  is the slope of change of the fiber volume fraction, and  $V_{f,o}$  is the fiber volume fraction at the inlet of the flow.

With the preforms positioned as shown in Figures 4 and 5, they attained the following values for the simulation:  $V_{f,o} = 0.5237$ ,  $V_f \in [0.1746, 0.5237]$ , and  $m = -4.365$ . The permeability in each point of the heterogeneous domain is computed by the Kozeny-Carman equation (9), using the quadratic equation shown in the Figure 3 to describe  $r_f^2/4k$  in terms of  $V_f$ .

## 8. Results

### 8.1. Case one: homogeneous domain–piecewise constant pressure

The input parameters for this simulation case are shown in Table 1. In this case of piecewise constant pressure regime, the history of the inlet pressure was obtained from the lectures of the manometer used in the experimental radial injection. For clarity purposes, the history of the inlet pressure acquired is plotted in Figure 6.

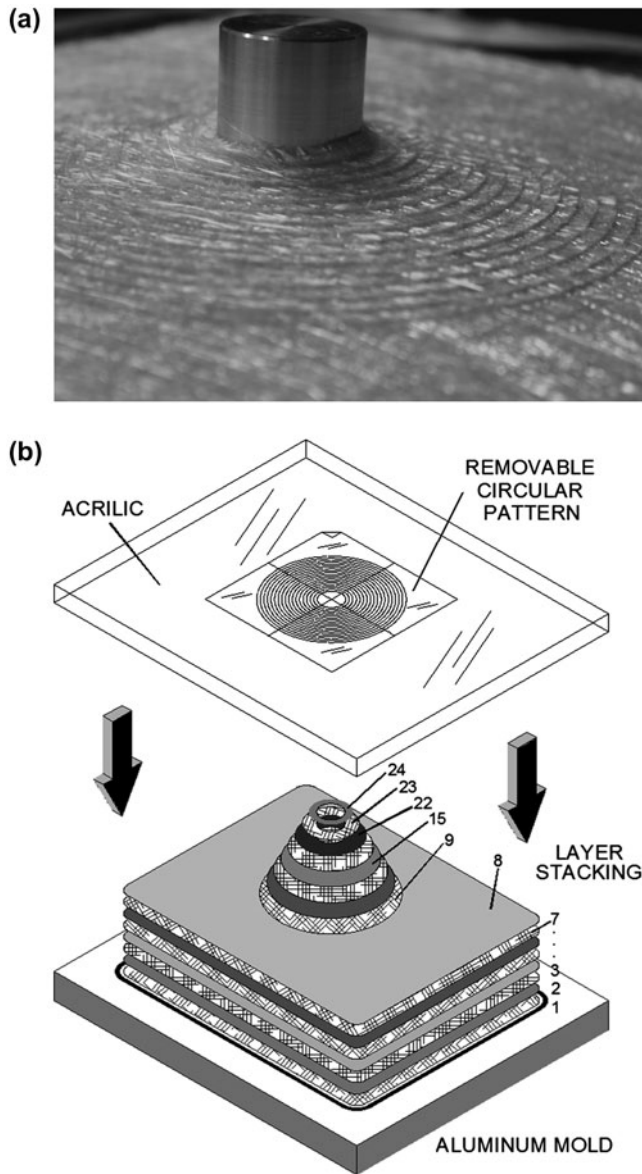


Figure 4. (a) Picture of the positioning of localized circular preforms. (b) Scheme of the heterogeneous domain.

The experimental radial injections were carried out as it was explained in experimental procedures section. In this case, the time of reference indicated by the chronometer was  $T_{\text{ref}} = 1:04:40$  mm:ss:cs. Table 5 is the comparison between the experimental and the BEM flow fronts at some instants of time and according to this table, the L1 relative error norm of BEM results regarding to experimental ones is 4.24%. The experimental position in each instant time was taken as the average of the positions in the four semi-axes. Several error sources can be identified to explain this difference. Some

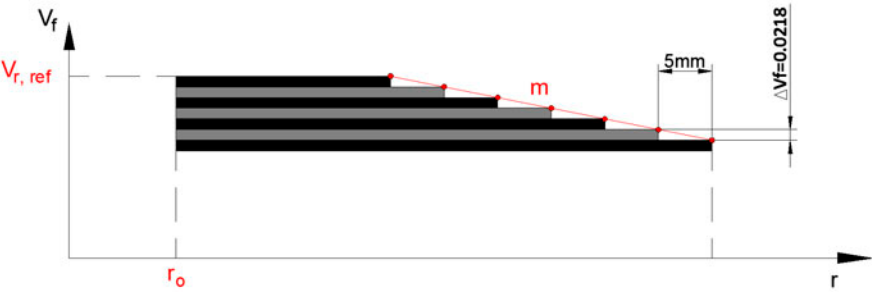


Figure 5. Quasi-linear radial change of the fiber volume fraction.

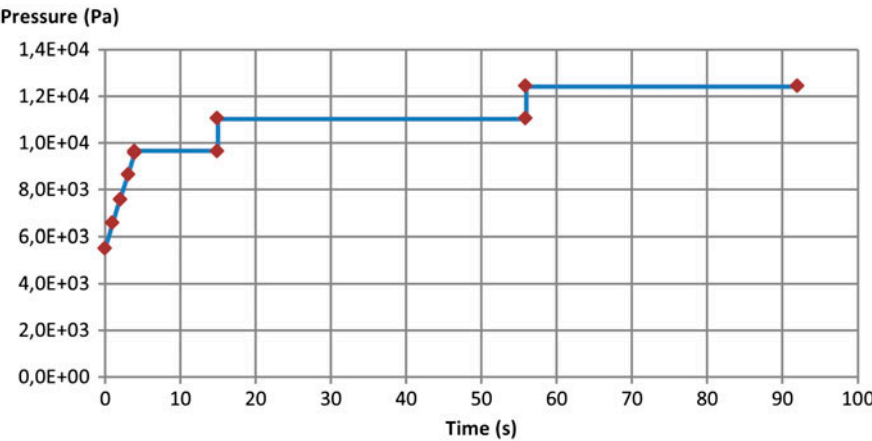


Figure 6. History of inlet pressure obtained from manometer Piecewise constant pressure.

Table 5. Comparison between BEM and experimental flow front positions piecewise constant pressure.

Time of reference in the chronometer (mm:ss:cs)	Instant of time in the chronometer (mm:ss:cs)	Instant of time (s)	BEM position (mm)	Experimental position (mm)	Norm. relative difference (%)
1:04:40	1:08:25	3.85	35.8	35.0	2.29
	1:19:46	15.06	55.2	55.5	0.54
	1:37:47	33.07	71.5	75.0	4.67
	1:57:27	52.87	84.0	90.0	6.67
	2:17:25	72.85	96.5	102.0	5.39
	2:34:71	90.31	104.5	111.0	5.85

of them are associated to the experimental assembly, like the uneven tighten of the transparent lid against the body of the mold with the perimeter screws and the deflection of that lid as a result of the low Young modulus of the acrylic ( $E = 6$  GPa). Other error sources are numeric and consist on the calculations of the integrals in the BEM

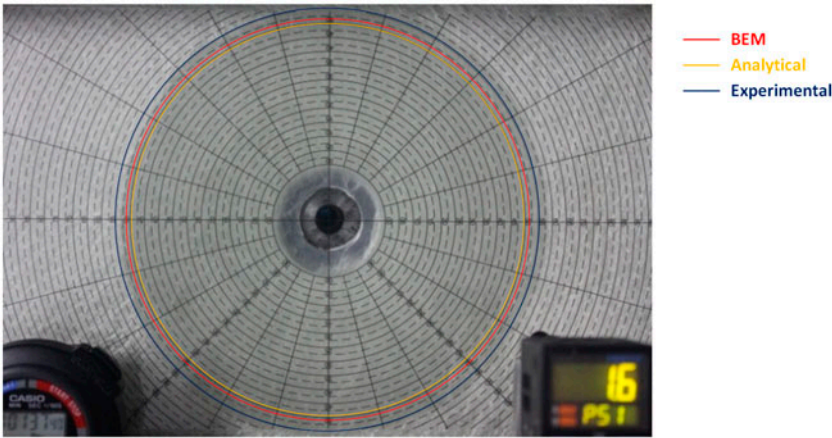


Figure 7. Comparison between analytical, BEM and experimental flow front positions for  $t = 33.07$  s- piecewise constant pressure.

Table 6. Comparison between analytical and BEM positions piecewise constant pressure.

Time (s)	Analytical flow front position (mm)	BEM flow front position (mm)	Norm. relative difference (%)
3.94	36.29	35.81	1.32
14.94	53.69	55.22	2.85
32.94	69.88	71.5	2.32
52.94	82.56	84.04	1.79
72.94	94.62	96.54	2.03
90.94	101.92	104.48	2.51

by Gaussian quadratures and on the treatment of the weak singularities by the Telles Transformation.[37] The other kind of error sources are related to the impregnation phenomenon as such and they could be a consequence of possible capillary effects presented during the divergent radial injection executed, because of the low mechanical pressures intentionally used in the experiment to obtain well-defined circular flow patterns. Figure 7 shows the saturated domain for the instant of time  $t = 33.07$  s calculated by BEM, analytical, and experimental methods, where the analytical position of the flow front was obtained using the following expression [40]:  $\left[ (r_f(t))^2 \cdot (2 \cdot \ln(r_f(t)/r_o) - 1) + (r_o)^2 \right] = 4/(\varepsilon\mu) \cdot K \cdot \int_0^t P_o(t) \cdot dt$ , where  $r_f(t)$  is the position of the flow front and  $P_o(t)$  is the inlet pressure.

In Table 6, analytical and BEM positions are compared. The L1 relative error norm is 2.14%, what is an indication of the accuracy of the BEM results for this case of study. In Figure 8, the behavior of the flow front velocity with the time predicted by the BEM program and the comparison with analytical results are plotted; it can be seen as an adequate agreement of the results. The analytical flow front velocity can be obtained from the following equation [38]:  $\langle V_f \rangle^f = -K/(\varepsilon\mu) \cdot P_o(t) \ln(r_o/r_f) \cdot 1/r_f$ .

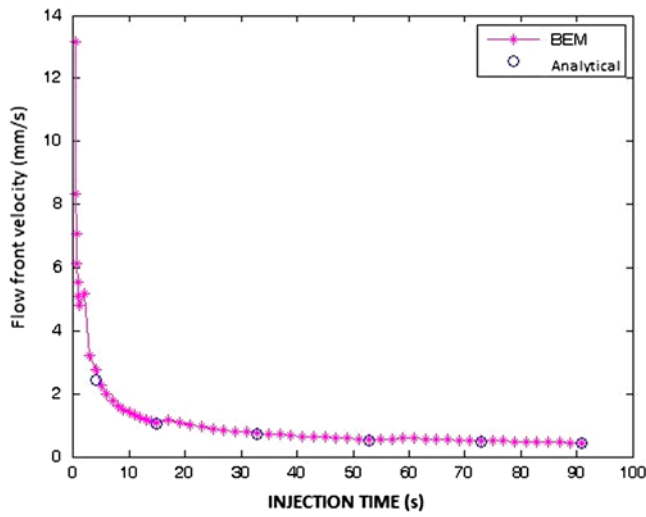


Figure 8. Flow front velocities- Piecewise constant pressure.

**8.2. Case 2: homogeneous domain–constant flow**

As it was mentioned before, the inlet flow in this case has been chosen in such a way that the saturated domain at the first time instants of the injection be similar to the one of the constant pressure regime of the case (one). As it is shown in Table 1, the selected inlet flow is  $Q_{in} = 4.94 \times 10^{-6} \text{ m}^3/\text{s}$ . The inlet pressure history calculated by BEM and the one computed analytically are plotted in the Figure 9, where an acceptable agreement between both results can be appreciated, L1 being the relative error norm of 1.14%. The equation used for the analytical calculation of the inlet pressure is

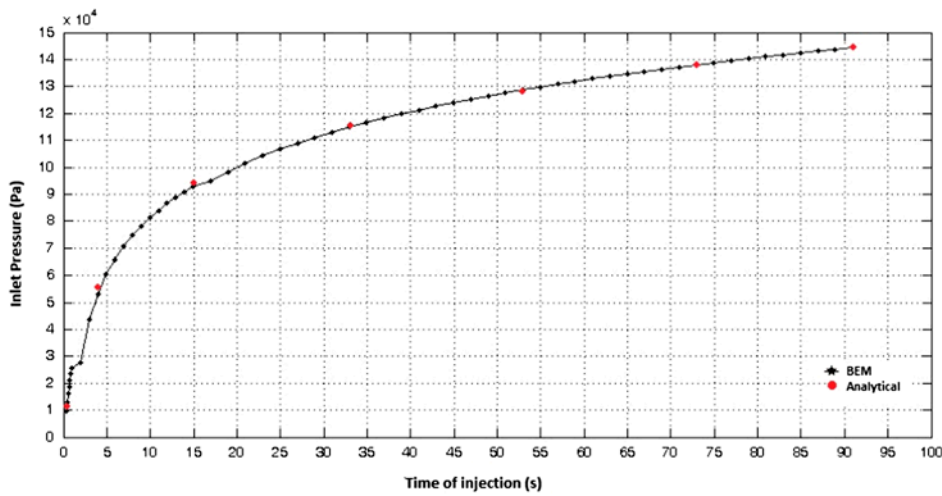


Figure 9. Inlet pressure history comparison between analytical and BEM results constant flow.

Table 7. Comparison among BEM and analytical flow front positions constant flow and among  $r_{f,BEM}$  of both regimes.

Instant time	Constant flow regime				Constant pressure (case 1)	
	$r_{f,anal}$ (mm)	$r_{f,BEM}$ (mm)	Norm. relative difference (%)	Position to average Inlet pressure ratio computed by BEM ( $m^3/N$ )	$r_{f,BEM}$ (mm)	Position to average inlet pressure ratio computed by BEM ( $m^3/N$ )
0.24	23.70	23.40	1.27	2.63E-06	23.2	4.21E-06
3.94	55.27	54.80	0.86	1.74E-06	35.81	4.93E-06
14.94	102.31	101.60	0.70	1.60E-06	55.22	6.12E-06
32.94	150.32	149.00	0.88	1.75E-06	71.5	7.08E-06
52.94	189.93	188.60	0.70	1.91E-06	84.04	8.04E-06
72.94	222.60	224.00	0.63	2.04E-06	96.54	8.83E-06
90.94	248.36	247.00	0.55	2.15E-06	104.48	9.31E-06

the following [39]:  $P_o(t) = -Q\mu/(2\pi hK) \cdot \ln(r_o/r_f)$ , where  $r_f$  can be calculated as  $r_f = (Q \cdot t/(\pi h \cdot \varepsilon) + r_o^2)^{1/2}$ .

In Table 7, it can be observed that there is good matching between BEM and analytical results for the positions of the flow front in the present case, L1 being the relative error norm of 0.8%. In the same table, they are shown the positions of the flow front computed by BEM for the piecewise constant pressure regime of the case one and it can be noticed that for a same instant of time, the difference between those positions and the ones of this case tends to increase, which is reasonable, because for two injections where the initial saturated domain is very similar, the constant flow injection originates flow front positions larger than the quasi-constant pressure injection positions. However, this does not mean that the injection of the case two is more efficient than the injection of case one, because the inlet pressures of the second case are very high regarding to the ones of the other case. To have an idea of the efficiency of the

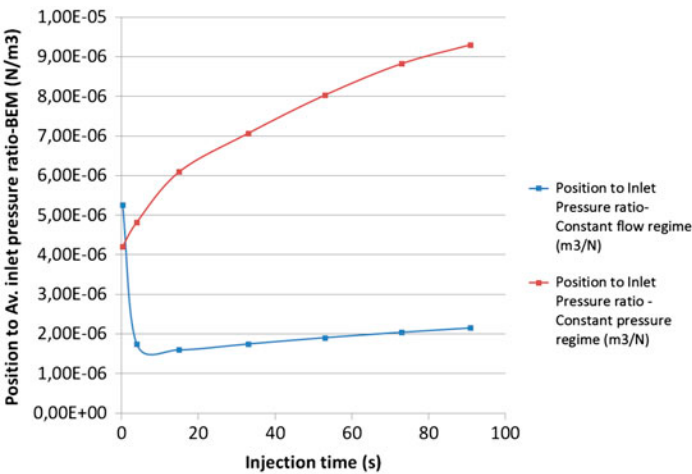


Figure 10. Comparison between Position to average inlet pressure ratios for constant pressure and constant flow regimes.



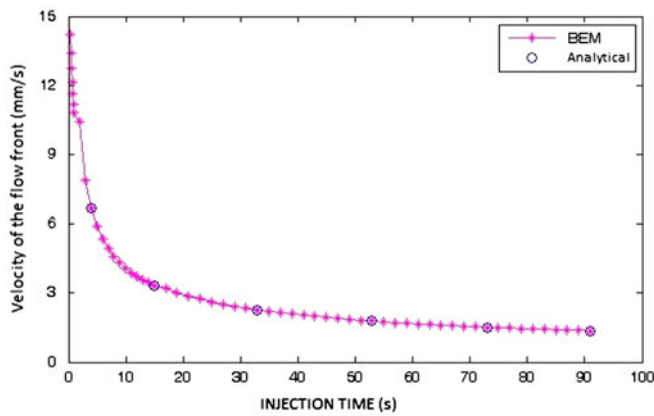


Figure 11. Flow front velocities- constant flow.

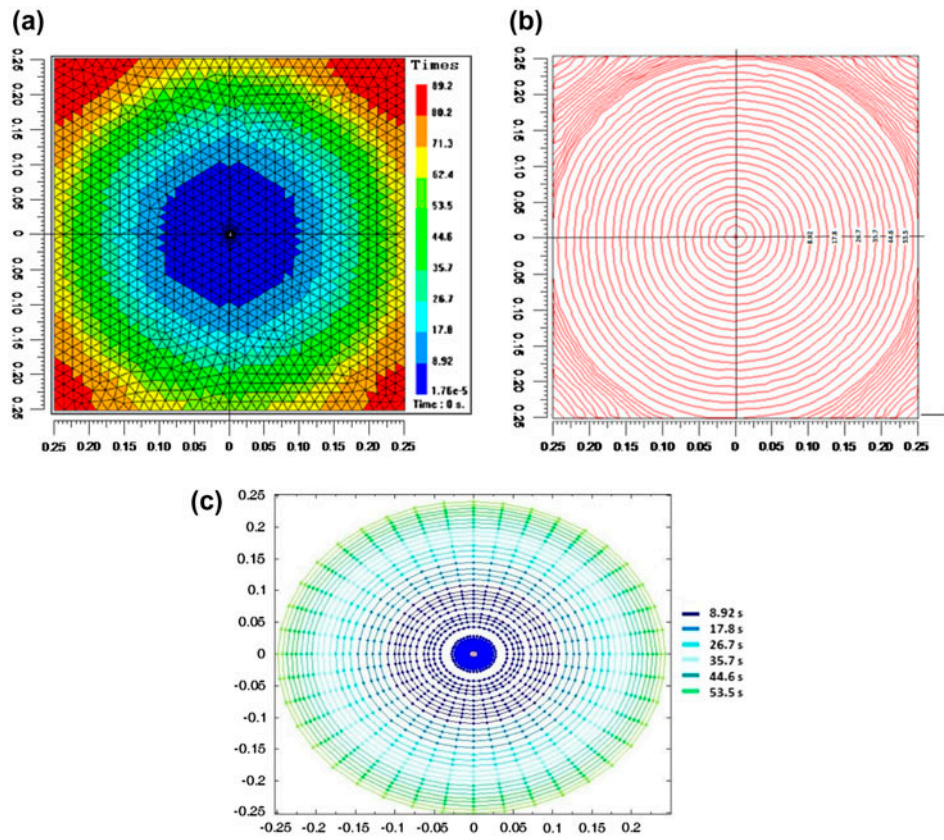


Figure 12. Flow front positions obtained with: (a) PAM-RTM [18], (b) BEM [18], and (c) BEM-present.

injections, it is introduced here the *Position to Average Inlet pressure ratio* for each instant of time, using the BEM results and the these ratios are plotted in Figure 10, where it can be appreciated that the injection of the case one is the most efficient of both injections, even though it generates lower flow front positions after the initial time instants of the injection. In this work, the average inlet pressure is taken as:  $P_{o,av}(t) = A(P_o, t)/t$ , where  $A(P_o, t)$  is the area under the curve in Figure 6 estimated by the trapezium rule.

The behavior of the velocity of the flow front for this case two is represented in Figure 11. The analytical values of this velocity can be computed using  $\langle V_f \rangle^f = Q/(2\pi \cdot r_f \cdot \varepsilon \cdot h)$ ; these values are shown in some instants of time for comparison purposes and it can be recognized the acceptable coincidence with the values computed by BEM (L1 relative error norm of 0.4%). If Figures 8 and 11 are compared, it can be noticed that the BEM code predicts similar initial velocities in both regimes. It is reasonable because the inlet flow in case two was selected to obtain an initial saturated domain similar to that of case one; however, a larger decrement of the velocity with the time in the initial instants of the injection is found when the injection is run at quasi-constant pressure (case one) than when it is run at constant flow (case two), and this is just the main cause that the flow front velocities in the rest of the injection keep lower in the quasi-constant pressure regime with respect to the constant flow regime.

### 8.3. Case three: homogeneous domain–constant pressure with gravitational effects

The same case study considered in [18] for constant pressure regime with gravitational effects is run in this case. The data are exposed in Table 2. In [18], two simulations were carried out. The first one was done using the commercial software PAM-RTM™, [14] which works with the non-conforming FEM/CV technique [10–13]; the other simulation was run with a pure BEM code designed by the authors of that work [18]. The major differences between that BEM formulation and the formulation proposed here

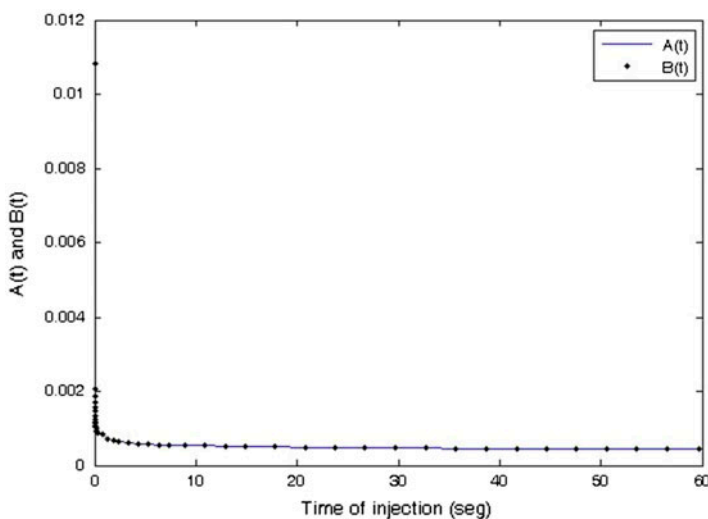


Figure 13. Mass conservation performance of the present BEM code.

Table 8. Comparison between DR-BEM and experimental flow front positions constant pressure.

Time of reference in the chronometer (mm:ss:cs)	Instant of time in the chronometer (mm:ss:cs)	Instant of time (s)	DR-BEM position	Experimental position	Norm. relative difference (%)
1:03:51	1:15:38	11.87	31.60	30.20	4.64
	1:55:78	52.27	45.00	43.00	4.65
	3:13:51	130.00	61.00	59.00	3.39
	5:14:19	250.68	78.60	75.50	4.11
	7:59:37	415.86	101.80	93.30	9.11

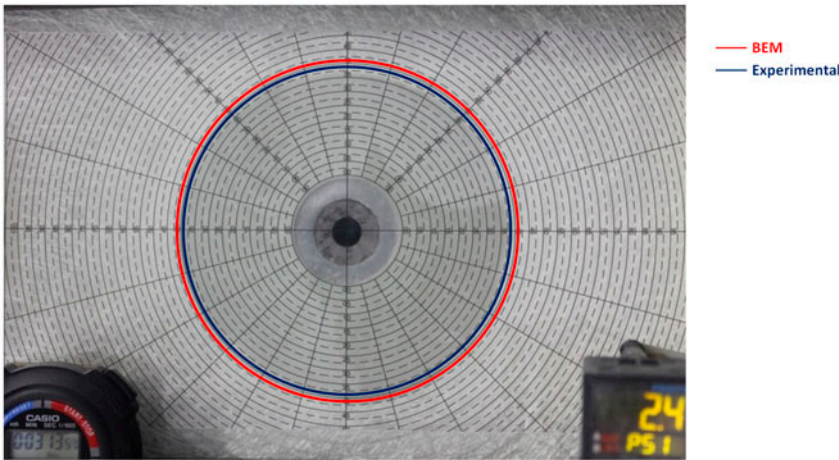


Figure 14. Comparison between DR-BEM and experimental flow front positions for  $t = 130$  s-constant pressure.

are: the fundamental solution employed here (see §2) is different from the solution used in [18]; in the present formulation the boundary is discretized in quadratic elements and the normal vectors are obtained using Catmull Rom splines to approximate the cloud of points,[25] while in the other formulation the elements are linear constants. In Figure 12, they compared the results of the three simulations. The present BEM formulation produces reasonable results for each instant of time, which are closer to the results obtained in PAM-RTM™. The L1 relative difference norm is: 1.13% regarding to PAM-RTM™ and 3.25% regarding to the other BEM formulation.[18]

The fulfillment of the mass conservation principle by part of the present BEM code can be checked with the results of the inlet and flow front velocities. In any instant of time, the following shall be complied by applying that principle:

$\int_0^{2\pi} V_o(\theta, t) r_o \cdot d\theta = \int_0^{2\pi} V_f(\theta, t) r_f(\theta, t) \cdot d\theta$ . Thus, doing  $A(t) = \int_0^{2\pi} V_o(\theta, t) r_o \cdot d\theta$  and  $B(t) = \int_0^{2\pi} V_f(\theta, t) r_f(\theta, t) \cdot d\theta$ , and solving the integrals numerically, in Figure 13, an adequate coincidence between both terms is shown concluding that the mass conservation principle is satisfactorily complied in the present BEM formulation.

#### 8.4. Case four: heterogeneous domain–constant pressure

In this case, the heterogeneous domain was created as it was exposed in permeability function in the heterogeneous domain section. The experimental position of the flow front in each instant of time was obtained by averaging the four flow front positions in the semi-axes, as it was done in the case one. L1 relative error norm of the BEM results with respect to the experimental ones, taking the instants of time in Table 8, is 5.18%. In Figure 14, the experimental flow front position is compared to the DR-BEM one for the instant of time  $t = 130$  s. Aside from the numerical and experimental error sources mentioned in the case one, which are also applicable to the present case, other causes of error can be identified here. First, the change of the fiber volume fraction with the radius is not exactly linear, but stepwise constant instead, that approximates better to a linear function as the radial gap between adjacent preforms and the areal weight of the preforms is smaller (see Figure 5). A second source of error comes from the fact that the term  $r_f^2/4k$  was determined experimentally, fitting the permeability measurements to the Kozeny-Carman equation to obtain the phenomenological expression exposed in Figure 3. As it is shown in the whisker plots of that figure, the scatter of the measurements of permeability leads to variations in the calculation of the term  $r_f^2/4k$  for each fiber volume fraction, which can be interpreted as errors by lack of repeatability of the permeability measurements; these errors can be attributed to both experimental errors and material variability.[40] An additional factor shall be considered in the permeability measurements: capillary effects are not taken into account and if the permeability experiments are conducted at very low injection pressures, these effects could be important during the experiments and the value of the interpolate permeability measured can be higher than the real value [41,42]; this could be a cause of the over-taking of the experimental positions by BEM positions in all instants of time in Table 8. The capillary effects during the permeability measurements can be estimated following the methodology proposed in [43], where a capillary-corrected permeability,  $K_{\text{corr}}$ , and the capillary pressure,  $P_c$ , are calculated for each fiber volume fraction. In this particular situation, the capillary effects during the measurements are quantified by calculating two factors:  $F_1 = (K_{\text{uns}} - K_{\text{corr}})/K_{\text{corr}}$  and  $F_2 = P_c/P_{\text{av}}$ . The former factor,  $F_1$ , accounts for the relative difference among the unsaturated permeability obtained in each experiment,  $K_{\text{uns}}$ , and the capillary-corrected permeability,  $K_{\text{corr}}$ ; as this factor is higher, the influence of the capillary effects on the experiment is higher too, but if this factor is

Table 9. Estimation of capillary effects in the permeability measurements.[44]

Fiber volume fraction	Average pressure (Pa)	$K_{\text{uns}}$ (m <sup>2</sup> )	$K_{\text{corr}}$ (m <sup>2</sup> )	$P_c$ (Pa)	(%)	$\frac{P_c}{P_{\text{av}}}$
0.551	148,000	4.603E-11	4.478E-11	12,129.60	2.798	8.196%
	93,000	4.914E-11			9.743	13.043%
0.455	114,000	1.931E-10	2.229E-10	-17,525.72	-13.366	NA
	96,000	1.804E-10			-19.064	NA
0.362	84,000	5.250E-10	6.619E-10	-19,704.59	-20.684	NA
	94,000	5.079E-10			-23.267	NA
0.257	60,000	1.455E-09	1.465E-09	1697.26	-0.672	2.829%
	51,000	1.311E-09			-10.502	3.328%
0.175	22,000	2.503E-09	2.846E-09	-1280.43	-12.046	NA
	51,000	2.61E-09			-8.286	NA

Table 10. Mass conservation performance of the present DR-BEM formulation-constant pressure.

Time instant (s)	$r_o$ (mm)	$r_f$ (mm)	$V_{f,o}$ (%)	$V_{f,f}$ (%)	$(u_{in}/u_f)_{iso}$	$(u_{in})_{DR-BEM}$ (mm/s)	$(u_f)_{DR-BEM}$ (mm/s)	$(u_{in}/u_f)_{BEM}$	Norm. relative difference $\frac{ (u_{in}/u_f)_{iso} - (u_{in}/u_f)_{DR-BEM} }{(u_{in}/u_f)_{iso}}$ (%)
11.87	20.0	31.6	52.37	47.31	1.75	2.02	1.025	1.97	12.74
52.27	20.0	45.0	52.37	41.46	2.77	1.31	0.452	2.90	4.80
129.99	20.0	61.0	52.37	34.47	4.20	1.07	0.260	4.11	1.96
250.67	20.0	78.6	52.37	26.79	6.04	0.95	0.185	5.14	14.99

negative, nothing can be concluded. The other factor,  $F_2$ , indicates how large is the capillary pressure regarding to the average injection pressure during the test; if the value of  $P_c$  computed by this method sets to a negative value, nothing can be concluded. The values of both factors are presented in Table 9 for the measurements of permeability conducted and it can be noticed that the capillary effects could have had a strong influence on the measurements of the cloth at  $V_f = 55.1\%$ ; taking into account only the factor  $F_1$ , the capillary effects presented in the measurements with  $V_f = 25.7\%$  probably have a weak influence on those measurements. To conclude with the possible additional sources of error of this case four, they can be mentioned the numerical errors that arise when the non-homogeneous term of Equation (3) is approximated by radial basis functions, like the thin plate splines employed in the present work.

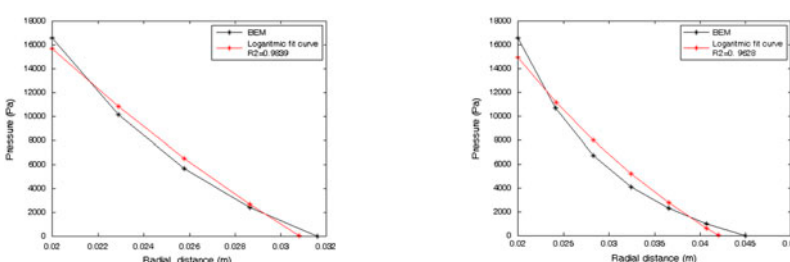
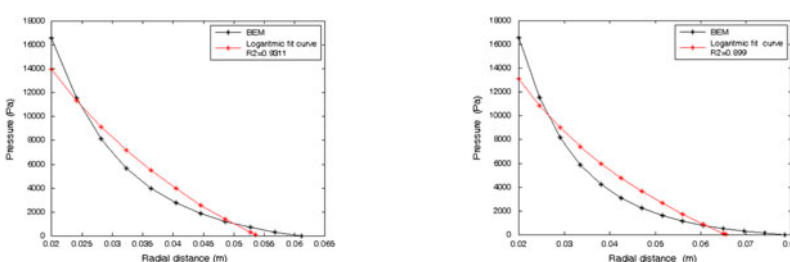
As it was done in the case three, in the present example, the mass conservation principle can be checked by calculating the ratio between the inlet pore velocity and the flow front pore velocity; if such a ratio complies the following expression, the principle is fulfilled:  $(u_o/u_f)_{\text{theo}} = r_f \cdot (1 - V_{f,f})/[r_o \cdot (1 - V_{f,o})]$ , where  $V_{f,o}$  is the fiber volume fraction at the inlet and  $V_{f,f}$  is the fiber volume fraction at the flow front. In Table 10, a comparison is presented among this theoretical ratio,  $(u_o/u_f)_{\text{theo}}$ , and the one computed from the DR-BEM results,  $(u_o/u_f)_{\text{DR-BEM}}$ . Important normalized relative differences can be appreciated, which is an indication of mass unbalances in the present DR-BEM formulation; this problem is also referenced in the boundary techniques employed by Voller and Peng [15] for the analysis of polymer filling molds. Further researches shall be conducted in order to study the influence of the number and location of the collocation points and of the use of more refined radial basis functions for the treatment of the non-homogeneous term, in the fulfillment of the mass conservation principle by the present DR-BEM code.

From the values of pressure computed for the interior collocation points using the DR-BEM code, it is obtained the radial variation of the pressure for several instants of time in Table 11. As it is demonstrated in [44], this radial variation fits to the following equation when the domain is homogeneous:  $P(r, t) = P_o(t)/\ln(r_o/r_f) \cdot \ln(r/r_f)$ . This means that for homogeneous domains and darcian flows in porous media, the behavior of the pressure with the radius is logarithmic for all instants of time. In this particular case of heterogeneous domain, the logarithmic curves that better fit the DR-BEM pressure profiles obtained by DR-BEM are also plotted in the Table 11 and according to the values and changes of the fitting parameter  $R^2$ , it can be concluded that the variation of pressure with the radius does not fit exactly to a logarithmic behavior and that the difference between the two behaviors is greater as the injection time increases. It is important to notice that the DR-BEM results indicate that, as the injection runs, pressure gradients in points near to the inlet tend to increase with respect to pressure gradients in points near to the flow front for this case of radial diminution,  $V_f$ . This can be clearly appreciated in the DR-BEM pressure field for  $t = 250.67$  s exposed in Figure 15.

Similar to the cases one and two, this case five and the case four share the same material and geometric parameters and the same range of fiber volume fraction, the only difference among them being the flow regime. And similar to the cases one and two, the inlet flow of this case five is selected to originate an initial saturated domain similar to the one of case four, which is conducted at constant pressure regime. This inlet flow is  $Q_{\text{in}} = 3.27 \times 10^{-6} \text{ m}^3/\text{s}$ .



Table 11. Change of pressure with the radius calculated by DR-BEM-constant pressure.

Instant of time=11.87 s	$V_{f,in}$ = 52.37%	$V_{f,f}$ = 47.31%	Instant of time=52.27 s	$V_{f,in}$ = 52.37%	$V_{f,f}$ = 41.46 %
					
Instant of time=129.99 s	$V_{f,in}$ = 52.37%	$V_{f,f}$ = 34.47%	Instant of time=250.67 s	$V_{f,in}$ = 52.37%	$V_{f,f}$ = 26.79%
					

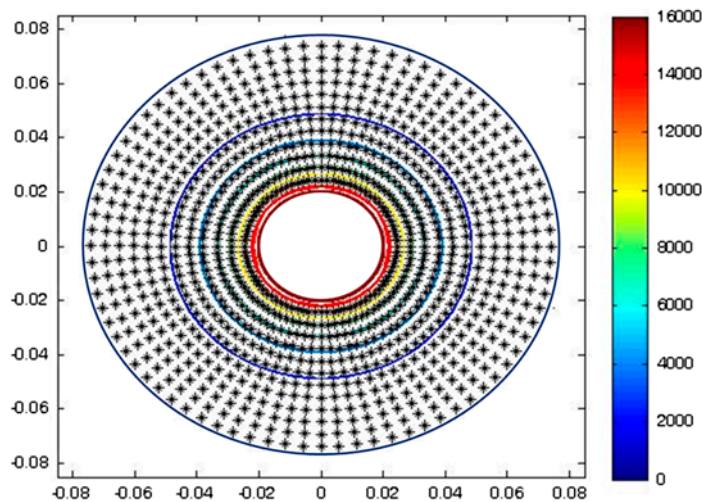


Figure 15. Pressure field for  $t = 250.67$  s- heterogeneous domain- constant pressure.

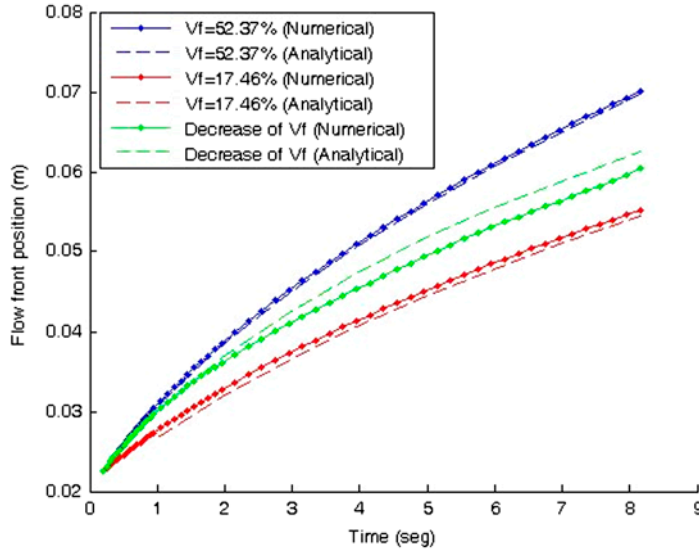


Figure 16. Flow front positions for both homogeneous and heterogeneous domains.

### 8.5. Case 5: heterogeneous domain–constant flow

The radial position of the flow front,  $r_f$ , can be computed analytically using the following equation:  $Q_{in} \cdot t = 2\pi h \left\{ (1 + m \cdot r_o - V_{f,o}) \left[ (r_f^2 - r_o^2)/2 \right] - m \left[ (r_f^3 - r_o^3)/3 \right] \right\}$

In Figure 16, it is shown that the change of the flow front position with the time of the injection for the present case of decrease in  $V_f$  and for two additional cases of homogeneous domain with  $V_f = 52.37\%$  (the maximum fiber volume fraction reached in the domain of the present case) and  $V_f = 17.46\%$  (the minimum fiber volume fraction reached in the domain of the present case). The analytical and numerical DR-BEM results are compared and important differences among those results can be recognized in the present example of decrease in  $V_f$ ; the L1 relative error norm is 2.99% and it can be attributed to numerical errors associated to the approximation of the non-homogeneous term of Equation (3) by the thin plate splines functions (§2) and using the quantity of the collocation points as it was specified in governing equations and numerical treatment by DR-BEM section. Other approximation functions with an optimal quantity of the collocation points can be implemented in future works in order to evaluate the reduction of the difference among analytical and DR-BEM results.

## 9. Conclusion

Two BEM approaches were implemented in the present work to simulate the infiltration process of isotropic fiber-reinforced preforms in the RTM process. The first one is a pure BEM approach with quadratic isoparametric elements, with a fundamental solution including the inlet radius of the preform and where the normals are computed based on Catmull Room splines. This approach was used to solve the governing equations in homogeneous domains. The matching of the numerical results of flow front positions, velocity profiles, and inlet pressure history to analytical, experimental, and numerical results of another authors shows that this approach is accurate enough to solve the



governing equations of the saturated domain for both constant pressure and constant flow regimes and that in further works it can be combined with more refined techniques for the track of the flow front advancement in complex shapes. The mass conservation principle is exactly fulfilled with this approach. Comparing the BEM results of both regimes, it was concluded that the piecewise constant pressure injection of this work is more efficient than the constant flow one, because although it generates lower flow front positions for all instants of time, the trade-off between those positions and power consumption is better in the former case.

The second approach consists on the implementation of the DR-BEM technique to consider the infiltration of non-homogeneous domains where the permeability changes as a known function; additional to the characteristics of the first pure BEM approach, in the present DR-BEM approach thin plate splines are also used as approximation functions to deal with the non-homogeneous term of the integral formulation. The adequate matching between numerical and experimental results and the mass unbalances presented in the constant pressure regime indicate that DR-BEM can be an accurate technique to solve the governing equation of non-homogeneous saturated domains, but that additional efforts, focused on using more refined approximation functions and/or on using more and/or better located collocation points, shall be done in order to exactly comply with the mass conservation principle. The coincidence between DR-BEM numerical and analytical results for the constant flow regime is acceptable, but it can be improved in the same way as the case of constant pressure regime. The radial pressure profiles obtained by DR-BEM indicate that the behavior of the pressure does not fit well to a logarithmic one, as in the case of homogeneous domains, and that, as the injection runs, the pressure gradients in points near to the inlet tend to increase with respect to the pressure gradients in points near to the flow front. Future experimental tests shall be conducted with the purpose of validate this prediction.

#### Nomenclature

$A(P_o, t)$	area under the curve of $P_o$ vs $t$ estimated by the trapezium rule	$n_x$	component $x$ of the normal vector
$A(t)$	integration of the pore velocity over the inlet boundary	$n_y$	component $y$ of the normal vector
$\alpha_j$	approximation coefficients	$N$	number of boundary collocation points
$B(t)$	integration of the pore velocity over the flow front boundary	$p$	pressure
$C_{\max}$	CFL coefficient	$P_c$	capillary pressure
$\varepsilon$	porosity	$P_{av}$	average injection pressure in an unidirectional unsaturated permeability test
$F_1$	factor accounting for the difference among the unsaturated and the capillary-corrected permeability	$P(r, t)$	pressure as a function of the radial position and the time
$F_2$	factor accounting for the difference among the capillary pressure and the average injection pressure of the permeability experiment.	$P_{o,av}(t)$	average inlet pressure in the radial injections
$f_j$	approximation functions	$P_o(t)$	inlet pressure as a function of time.
$\underline{g}$	gravitational acceleration	$\rho$	density
$\phi$	Dirichlet-type boundary condition	$q(x)$	normal derivative of the transformed potential

$\emptyset(x)$	potential as a function of the space	$Q$	injected flow rate
$\xi$	source point	$\bar{q}_{in}$	Neuman-type boundary condition at the inlet
$h$	thickness of the cavity	$\hat{q}_j(x)$	normal derivative of the adjacent harmonic function
$K(x)$	permeability as a function of the space	$q^*(\xi, x)$	normal derivative of the fundamental solution
$K_{uns}$	unsaturated permeability	$r$	radial position of any point in the saturated domain
$K_{corr}$	capillary-corrected permeability	$r_o$	radius of the inlet point
$L$	number of interior collocation points	$r^*$	distance between the field point and the source point
$m$	slope of change of the fiber volume fraction	$r_f(t)$	position of the flow front
$r_{f,anal}$	analytical position of the flow front	$\mu$	viscosity of the injected liquid
$r_{f,BEM}$	BEM position of the flow front	$V_f$	fiber volume fraction
$r_f^2/4k$	Kozeny coefficient	$V_{f,o}$	fiber volume fraction at the inlet of the flow.
$S$	Surface surrounding the saturated porous domain	$V_{f,f}$	fiber volume fraction at the flow front
$t$	instant of time	$V_f(r)$	fiber volume fraction at determined radial position
$T_{ref}$	reference time to start the experiments	$V_o(\theta, t)$	inlet velocity as a function of angular position and time
$\Delta t$	Interval of time to advance the flow front	$V_f(\theta, t)$	velocity of the flow front as a function of angular position and time
$\Delta x_t$	increment in $x$ to compute $\Delta t$ using CFL condition	$\langle V_f \rangle^f$	pore velocity
$\Delta y_t$	increment in $y$ to compute $\Delta t$ using CFL condition	$\mathbf{x}$	field point
$u_{in}$	Potential at the inlet corresponding to the Robin boundary condition	$x_t$	position of the flow front in $x$ at time $t$
$u(x)$	transformed potential as a function of space	$x_{t+\Delta t}$	position of the flow front in $x$ at time $t + \Delta t$
$\hat{u}_j(x)$	adjacent harmonic function of the approximation function	$x^j$	collocation point for the DR-BEM
$(u_o/u_f)_{theo}$	theoretical ratio between the inlet pore velocity and the flow front pore velocity	$y_t$	position of the flow front in $y$ at time $t$
$(u_o/u_f)_{DR-BEM}$	ratio between the inlet pore velocity and the flow front pore velocity obtained from DR-BEM results	$y_{t+\Delta t}$	position of the flow front in $y$ at time $t + \Delta t$
$\bar{u}(x_1, x_2)$	transformed Dirichlet boundary condition	$\Omega$	saturated porous domain
$u^*(\xi, \mathbf{x})$	fundamental solution	$z$	vertical coordinate

## Acknowledgements

The financial support provided by Instituto Tecnológico Metropolitano under the research internal project P10220 made this work possible.

## References

- [1] Trochu F, Gauvin R. Limitations of a boundary-fitted finite difference method for the simulation of the resin transfer molding process. *J. Reinf. Plast. Compos.* 1992;11:772–786.

- [2] Coulter JP, Guceri SI. Resin impregnation during the manufacturing of composite materials subject to prescribed injection rate. *J. Reinf. Plast. Compos.* 1988;7:200–219.
- [3] Tamma KK, Mohan RV, Ngo NO. An overview of recent developments and advances in Resin transfer moulding of thin/thick composites structures. ARO report; 1994.
- [4] Mohan RV, Ngo NO, Tamma KK, Fickie KD. On a pure finite element base methodology for Resin Transfer Mold filling simulations. 9th International Conference. Numerical methods in thermal problems. Vol. IX, 1995;39:1287–1310.
- [5] Fracchia CA, Castro J, Tucker CL. A finite element/control volume simulation of resin transfer mold filling. *Am. Soc. Compos.* 1989;157–166.
- [6] Bruschke MV, Advani SG. A finite element/control volume approach to mold filling in anisotropic porous media. *Polym. Compos.* 1990;11:398–405.
- [7] Liu B, Bickerton S, Advani SG. Modeling and simulation of resin of resin transfer molding (RTM)- gate control, venting and dry spot prediction. *Compos. Part A Appl. Sci. Manuf.* 1992;27:135–141.
- [8] Bruschke MV, Advani SG. A numerical approach to model non-isothermal, viscous flow with free surfaces through fibrous media. *Int. J. Numer. Methods Fluids.* 1994;19:515–603.
- [9] Center for Composites Materials of University of Delaware. ‘LIMS’, University of Delaware. 2011. Available from: <http://www.ccm.udel.edu/Pubs/techbriefs/LIMS.pdf>
- [10] Trochu F, Gauvin R, Gao D-M. Numerical analysis of the resin transfer molding process by the finite element method. *Adv. Polym. Technol.* 1993;12(4):329–342.
- [11] Ruiz E, Achim V, Trochu F. Coupled non-conforming finite element and finite difference approximation based on laminate extrapolation to simulate liquid composite molding processes. Part I: isothermal flow. *Sci. Eng. Compos. Mater.* 2011;14:85–112.
- [12] Diallo ML, Gauvin R, Trochu F. Experimental analysis and simulation of flow through multi-layer fiber reinforcements in liquid composite molding. *Polym. Compos.* 1998;19:246–256.
- [13] Ruiz E, Achim V, Soukane S, Trochu F, Breard J. Optimization of injection flow rate to minimize micro/macro-voids formation in resin transfer molded composites. *Compos. Sci. Technol.* 2006;66:475–486.
- [14] E.S.I. Group International Ltd. PAM-RTM. Available from: <http://www.esi-group.com/products/composites-plastics/pam-rtm>
- [15] Voller VR, Peng S. An algorithm for analysis of polymer filling of molds. *Polym. Eng. Sci.* 1995;35:1758–1765.
- [16] Um M-K, Lee W. A study on the mold filling process in resin transfer molding. *Polym. Eng. Sci.* 1991;31(11):765–771.
- [17] Soukane S, Trochu F. Application of the level set method to the simulation of resin transfer molding. *Compos. Sci. Technol.* 2006;66:1067–1080.
- [18] Gantois R, Cantarel A, Dusserre G. Mold filling simulation of resin transfer molding combining BEM and level set method. *Appl. Mech. Mater.* 2011;62:57–65.
- [19] Yoo Y-E, II Lee W. Numerical simulation of the resin transfer mold filling process using the boundary element method. *Poly.* 1996;17:368–374.
- [20] Martínez MA, Cueto E, Doblaré M, Chinesta F. Natural element meshless simulation of flows involving short fiber suspensions. *J. Nonnewton. Fluid Mech.* 2003;115:51–78.
- [21] García JA, Gascón Li, Cueto E, Ordeig I, Chinesta F. Meshless methods with application to Liquid Composite Molding simulation. *Comput. Methods Appl. Mech. Eng.* 2009;198:2700–2709.
- [22] González D, Cueto E, Chinesta F, Doblaré M. A natural element updated Lagrangian strategy for free-surface fluid dynamics. *J. Comput. Phys.* 2007;223:127–150.
- [23] Jiang F, Oliveira MSA, Sousa ACM. Mesoscale SPH modeling of fluid flow in isotropic porous media. *Comput. Phys. Commun.* 2007;176:471–480.
- [24] Brebbia CA, Dominguez J. Boundary elements: an introductory course. 2nd ed. Southampton and Boston: Comput. Mech. Publications and McGraw-Hill; 1992. p. 317.
- [25] Twigg C. Catmull-Rom splines. Available from: <http://www.cs.cmu.edu/~fp/courses/graphics/asst5/catmullRom.pdf>
- [26] Šarler B, Perko J, Gobin D, Goyeau B, Power H. Dual reciprocity boundary element method solution of natural convection in Darcy–Brinkman porous media. *Eng. Anal. Bound. Elem.* 2004;28(1):23–41.

- [27] Partridge PW, Brebbia CA. The dual reciprocity boundary element method. New York (NY): Computational Mechanics Publications; 1992. p. 276.
- [28] Lennon GP. In: Boundary element analysis of flow in heterogeneous porous media. In ASCE/HYD Specialty Conference. New York (NY): Hydraulic Division, ASCE; 1984.
- [29] Chen AH. Heterogeneities in flows through porous media by the boundary element method. Topics in boundary element Research. Springer-Verlag. 1987;4:129–144.
- [30] Whitaker S. The method of volume averaging. Theory and applications of transport in porous media. London: Kluwer Academics; 1999.
- [31] Hamaguchi S. A shock-tracking algorithm for surface evolution under reactive-ion etching. J. Appl. Phys. 1993;74:5172–5184.
- [32] Sethian JA. Level set methods and fast marching methods: evolving interfaces in computational geometry, fluid mechanics, computer vision and material science. London: Cambridge University Press; 2005. p. 379.
- [33] Alms JB, Correia NC, Advani SG, Ruiz E. Experimental procedures to run longitudinal injections to measure unsaturated permeability of LCM reinforcements. Available from: [http://cchp.meca.polymtl.ca/fichiers/permeabilityBenchmarkII/PermBenchmark\\_a4.pdf](http://cchp.meca.polymtl.ca/fichiers/permeabilityBenchmarkII/PermBenchmark_a4.pdf)
- [34] Ferland P, Guittard D, Trochu F. Concurrent methods for permeability measurement in resin transfer molding. Polym. Compos. 2004;17:149–158.
- [35] Demaria C, Ruiz E, Trochu F. In-plane anisotropic permeability characterization of deformed woven fabrics by unidirectional injection. Part II: prediction model and numerical simulations. Polym. Compos. 2007;28:812–827.
- [36] Gutowski TG. Advanced composites manufacturing. New York (NY): Wiley; 1997.
- [37] Telles JCF. A self-adaptive co-ordinate transformation for efficient numerical evaluation of general boundary element integrals. Int. J. Numer. Methods Eng. 1987;24:959–973.
- [38] Lundström TS, Stenberg R, Bergström R, Partanen H, Birkeland PA. In-plane permeability measurements: a nordic round-robin study. Compos. Part A Appl. Sci. Manuf. 2000;31:29–43.
- [39] Chan AW, Larive DE, Morgan RJ. Anisotropic permeability of fiber preforms: constant flow rate measurement. J. Compos. Mater. 1993;27:996–1008.
- [40] Arbter R, Beraud JM, Binetruy C, Bizet L, Bréard J, Comas-Cardona S, Demaria C, Endruweit A, Ermanni P, Gommer F, Hasanovic S, Henrat P, Klunker F, Laine B, Lavanchy S, Lomov SV, Long AC, Michaud V, Morren G, Ruiz E, Sol H, Trochu F, Verleye B, Wietgreffe M, Wu W, Ziegmann G. Experimental determination of the permeability of textiles: a benchmark exercise. Compos. Part A Appl. Sci. Manuf. 2011;42:1157–1168.
- [41] Visconti IC, Langella M, Durante M. The influence of injection pressure on the permeability of unidirectional fibre preforms in RTM. In: 8th European Conference on Composite Materials; ECCM-8; 1998 Aug; Lisbon, Portugal. p. 737–743.
- [42] Ahn KJ, Seferis JC, Berg JC. Simultaneous measurements of permeability and capillary pressure of thermosetting matrices in woven fabric reinforcements. Polym. Compos. 1991;12:146–152.
- [43] Amico S, Lekakou C. An experimental study of the permeability and capillary pressure in resin-transfer moulding. Compos. Sci. Technol. 2001;61:1945–1959.
- [44] Adams KL, Russel WB, Rebenfeld L. Radial penetration of a viscous liquid into a planar anisotropic porous medium. Int. J. Multiph. Flow. 1988;14:203–215.